

See discussions, stats, and author profiles for this publication at: <https://www.researchgate.net/publication/44610327>

Embedded Microstructures by Electric-Field-Induced Pattern Formation in Interacting Thin Layers

ARTICLE *in* LANGMUIR · JULY 2010

Impact Factor: 4.46 · DOI: 10.1021/la100968p · Source: PubMed

CITATIONS

11

READS

47

3 AUTHORS:



[Samanvaya Srivastava](#)

Cornell University

15 PUBLICATIONS 228 CITATIONS

SEE PROFILE



[Dipankar Bandyopadhyay](#)

Indian Institute of Technology Guwahati

59 PUBLICATIONS 534 CITATIONS

SEE PROFILE



[Ashutosh Sharma IITK](#)

Indian Institute of Technology Kanpur

334 PUBLICATIONS 7,407 CITATIONS

SEE PROFILE

Embedded Microstructures by Electric-Field-Induced Pattern Formation in Interacting Thin Layers

Samanvaya Srivastava,^{†,||} Dipankar Bandyopadhyay,[‡] and Ashutosh Sharma^{*,†,§}

[†]Department of Chemical Engineering, Indian Institute of Technology, Kanpur, India, [‡]Department of Chemical Engineering, Indian Institute of Technology, Guwahati, India, and [§]School of Mechanical Engineering, Yeungnam University, Gyongsan, South Korea. ^{||}Present address: School of Chemical and Biomolecular Engineering, Cornell University, Ithaca, New York 14853-5201.

Received March 9, 2010. Revised Manuscript Received May 1, 2010

Electric-field-induced interfacial instabilities and pattern formation in a pair of interacting thin films are analyzed on the basis of linear stability analysis and long-wave nonlinear simulations. The films are coated onto two parallel plate electrodes and separated by an air gap between them. A linear stability analysis (LSA) is carried out for viscoelastic films to show that the ratios of material properties to films thickness control the length scale and timescale significantly and the presence of the second layer increases the overall capacitance and thus can lead to a smaller length scale as compared to the instability in a single film. Long-wave nonlinear analysis for interacting viscous layers indicates that the instabilities are always initiated by the antiphase squeezing rather than the in-phase bending mode of deformation at the interfaces. Nonlinear simulations on patterned electrodes show that this novel geometry for electric field patterning can be employed to generate intricate, embedded 3-D periodic patterns and to miniaturize patterns. Simulations are presented for e-molding of a number of periodic self-organized patterns such as pincushion structures, straight/corrugated embedded microchannels, and microbubbles. A few interesting examples are also shown where (1) the pathway of evolution changes without altering the equilibrium morphology when kinetic parameters such as viscous forces are changed and (2) the self-organized equilibrium morphology does not reproduce the underlying patterns on the electrodes.

1. Introduction

Instabilities on the surfaces of thin polymer films lead to mesopatterns that are of scientific and technological importance. Patterned polymer surfaces find applications in diverse areas such as electronic device fabrication,¹ optoelectronics,² biotechnology,^{3,4} and microfluidic devices.⁵ Recent reviews^{6–12} discuss microtextured surfaces exhibiting superhydrophobicity, self-cleaning, drag-reducing, antifouling, and antistick properties. Furthermore, instabilities of thin polymer films serve as prototypes for studying

various scientific issues, for example, dewetting,^{13–62} adhesion and debonding,^{63–71} friction, intermolecular forces, adsorption, and phase transitions. Thus, extensive efforts have been devoted

*Author to whom correspondences should be addressed. Tel: +91-512-259 7026. Fax: +91-512-259 0104. E-mail: ashutos@iitk.ac.in.

- (1) Hu, Z.; Tian, M.; Nysten, B.; Jonas, A. M. *Nat. Mater.* **2008**, *8*, 62.
- (2) Nie, Z.; Kumacheva, E. *Nat. Mater.* **2008**, *7*, 277.
- (3) Langer, R.; Tirrell, D. A. *Nature* **2004**, *428*, 487.
- (4) Jeong, K. H.; Kim, J.; Lee, L. P. *Science* **2006**, *312*, 557.
- (5) Squires, T. M.; Quake, S. R. *Rev. Mod. Phys.* **2005**, *77*, 977.
- (6) Ball, P. *Nature* **1999**, *400*, 507.
- (7) Nakajima, A.; Hashimoto, K.; Watanabe, T. *Monatsh. Chem.* **2001**, *132*, 31.
- (8) Lafuma, A.; Quéré, D. *Nat. Mater.* **2003**, *2*, 457.
- (9) Blossey, R. *Nat. Mater.* **2003**, *2*, 301.
- (10) van der Wal, P.; Steiner, U. *Soft Matter* **2007**, *3*, 426.
- (11) Li, X.-M.; Reinholdt, D.; Crego-Calama, M. *Chem. Soc. Rev.* **2007**, *36*, 1350.
- (12) Stuart, M. A. C.; Huck, W. T. S.; Genzer, J.; Müller, M.; Ober, C.; Stamm, M.; Sukhorukov, G. B.; Szleifer, I.; Tsukruk, V. V.; Urban, M.; Winnik, F.; Zauscher, S.; Luzinov, I.; Minko, S. *Nat. Mater.* **2010**, *9*, 101.
- (13) Ruckenstein, E.; Jain, R. K. *J. Chem. Soc., Faraday Trans. 2* **1974**, *70*, 132.
- (14) De Gennes, P. G. *Rev. Mod. Phys.* **1985**, *57*, 827.
- (15) Reiter, G. *Phys. Rev. Lett.* **1992**, *68*, 75.
- (16) Brochard-Wyart, F.; Martin, P.; Redon, C. *Langmuir* **1993**, *9*, 3682.
- (17) Sharma, A. *Langmuir* **1993**, *9*, 861.
- (18) Reiter, G. *Langmuir* **1993**, *9*, 1344.
- (19) Oron, A.; Davis, S. H.; Bankoff, S. G. *Rev. Mod. Phys.* **1997**, *69*, 931.
- (20) Sharma, A.; Khanna, R. *Phys. Rev. Lett.* **1998**, *81*, 3463.
- (21) Ghatak, A.; Khanna, R.; Sharma, A. J. *Colloid Interface Sci.* **1999**, *212*, 483.
- (22) Yerushalmi-Rozen, R.; Kerle, T.; Klein, J. *Science* **1999**, *285*, 1254.
- (23) Oron, A.; Bankoff, S. G. *J. Colloid Interface Sci.* **1999**, *218*, 152.
- (24) Thiele, U.; Velarde, M.; Neuffer, K. *Phys. Rev. Lett.* **2001**, *87*, 016104.
- (25) Sharma, A.; Mittal, J. *Phys. Rev. Lett.* **2002**, *89*, 186101.
- (26) Narsimhan, G. *J. Colloid Interface Sci.* **2005**, *287*, 624.
- (27) Bandyopadhyay, D.; Gulabani, R.; Sharma, A. *Ind. Eng. Chem. Res.* **2005**, *44*, 1259.

- (28) Yang, M. H.; Hou, S. Y.; Chang, Y. L.; Yang, A. C.-M. *Phys. Rev. Lett.* **2006**, *96*, 066105.
- (29) Xu, L.; Shi, T. F.; An, L. J. *Langmuir* **2007**, *23*, 9282.
- (30) Konnur, R.; Kargupta, K.; Sharma, A. *Phys. Rev. Lett.* **2000**, *84*, 931.
- (31) Zope, M.; Kargupta, K.; Sharma, A. *J. Chem. Phys.* **2001**, *114*, 7211.
- (32) Kargupta, K.; Sharma, A. *Phys. Rev. Lett.* **2001**, *86*, 4536.
- (33) Kargupta, K.; Sharma, A. *J. Chem. Phys.* **2002**, *116*, 3042.
- (34) Kargupta, K.; Sharma, A. *Langmuir* **2003**, *19*, 5153.
- (35) Kargupta, K.; Sharma, A. *J. Colloid Interface Sci.* **2002**, *245*, 99.
- (36) Kargupta, K.; Sharma, A. *Langmuir* **2002**, *18*, 1893.
- (37) Brusch, L.; Kühne, H.; Thiele, U.; Bär, M. *Phys. Rev. E* **2002**, *66*, 011602.
- (38) Thiele, U.; Brusch, L.; Bestehorn, M.; Bär, M. *Eur. Phys. J. E* **2003**, *11*, 255.
- (39) Kao, J. C. T.; Golovin, A. A.; Davis, S. H. *J. Colloid Interface Sci.* **2006**, *303*, 532.
- (40) Simmons, D.; Chauhan, A. J. *Colloid Interface Sci.* **2006**, *295*, 472.
- (41) Saprykin, S.; Trevelyan, P. M. J.; Koopmans, R. J.; Kalliadasis, S. *Phys. Rev. E* **2007**, *75*, 026306.
- (42) Lenz, R. D.; Kumar, S. *J. Fluid Mech.* **2007**, *571*, 33.
- (43) Bandyopadhyay, D.; Sharma, A.; Rastogi, C. *Langmuir* **2008**, *24*, 14048.
- (44) Reiter, G.; Auroy, P.; Auvray, L. *Macromolecules* **1996**, *29*, 2150.
- (45) Mayer, E.; Braun, H. G. *Macromol. Mater. Eng.* **2000**, *276/277*, 44.
- (46) Sehgal, A.; Ferreira, V.; Douglas, J. F.; Amis, E. J.; Karim, A. *Langmuir* **2002**, *18*, 7041.
- (47) Zhang, Z.; Wang, Z.; Xing, R.; Han, Y. *Surf. Sci.* **2003**, *539*, 129.
- (48) Wunnicke, O.; Müller-Buschbaum, P.; Wolkenhauer, M.; Lorenz-Haas, C.; Cubitt, R.; Leiner, V.; Stamm, M. *Langmuir* **2003**, *19*, 8511.
- (49) Wang, X.; Ostblom, M.; Johansson, T.; Inganäs, O. *Thin Solid Films* **2004**, *449*, 125.
- (50) Luo, C.; Xing, R.; Han, Y. *Surf. Sci.* **2004**, *552*, 139.
- (51) Zhang, X.; Xie, F.; Tsui, O. K. C. *Polymer* **2005**, *46*, 8416.
- (52) Kim, D. H.; Kim, M. J.; Park, J. Y.; Lee, H. H. *Adv. Funct. Mater.* **2005**, *15*, 1445.
- (53) Mukherjee, R.; Gonuguntla, M.; Sharma, A. *J. Nanosci. Nanotechnol.* **2007**, *7*, 2069.
- (54) Kwon, S. J. *J. Appl. Phys.* **2006**, *99*, 063503.
- (55) Wei, J. H.; Coffey, D. C.; Ginger, D. J. *Phys. Chem. B* **2006**, *110*, 24324.
- (56) Baralia, G. G.; Filiate, C.; Nysten, B.; Jones, A. M. *Adv. Mater.* **2007**, *19*, 4453.
- (57) Martin, C. P.; Blunt, M. O.; Pauliac-Vaujour, E.; Stannard, A.; Moriarty, P. *Phys. Rev. Lett.* **2007**, *99*, 116103.
- (58) Julthongpipit, D.; Zhang, W. H.; Douglas, J. F.; Karim, A.; Fasolka, M. J. *Soft Matter* **2007**, *3*, 613.

to improving the understanding of instabilities in thin polymer films.

Among the existing patterning techniques, self-organized dewetting of ultrathin polymer films under the influence of intermolecular forces generates a collection of droplets on flat surfaces.^{13–29} Previous theoretical^{30–43} and experimental^{44–62} studies suggest that the ordering of the dewetted microstructures can be controlled and large-area periodic patterns can be obtained under certain conditions by imposing physical or chemical patterns on the surface of the solid substrate. Recent studies show that, similar to dewetting-induced pattern formation, the application of an electric field across the free surface of a polymer film can be another simple method for

fabricating micropatterns.^{72–109} A variety of microstructures including regularly packed,^{72–85} hierarchical,⁷⁸ and phase-inverted⁸² columnar structures are formed on the surfaces of thin polymer films ($< 10\ \mu\text{m}$) under the influence of an externally applied electric field when the destabilizing electric field forces overcome the restoring surface tension force. In this context, a number of interesting systems have been investigated: (i) a single dielectric liquid film,^{72,73,75,83–85,88,90,93,94,98} an elastic film,^{86,91,103} or a conducting film^{93,100,104,105} under air, (ii) a composite of a dielectric and a conducting liquid,⁹² (iii) a bilayer of dielectric⁷⁴ or leaky dielectric^{106,107} liquids, (iv) a bilayer of viscous or elastic films under air,^{78,82,87,108} and (v) the use of an AC electric field for patterning.¹⁰⁹ Some studies^{83–85,89,98} also reveal that patterned electrodes can direct the large-scale alignment of microstructures, which indicates the potential of the electric field as a tool of microfabrication in the creation of large-area surface patterns. Compared to the pattern formation and its control in ultrathin ($< 50\ \text{nm}$) films by the van der Waals force,^{13–29} electric field induced patterning provides far greater control over the destabilizing force and patterns, including the use of thicker films.

Apart from the systems mentioned previously, a set of two interacting polymer films with a thin air gap between them is another system that has been considered recently.^{110–113} However, in these studies, only the instabilities engendered in purely elastic films by the intermolecular forces were considered, which require stringent control of the air gap down to the nanometer scale. The application of an external electric field in a viscoelastic¹¹⁴ or viscous film is another alternative to exerting greater and longer-ranged control over the destabilizing force and resulting patterns.^{72–109} In the present work, we propose a configuration of two interacting linearly viscoelastic soft films and viscous films under the influence of an externally applied electric field to explore the possibility of fabricating 3-D embedded microstructures such as an array of channels and bubbles and to extend our control over the length scale and timescale of the microstructures. This is in contrast to the extensively studied instability of a single film that can produce only shallow surface structures. There has been great recent interest in the fabrication of a buried array of microbubbles and channels with a combination of top-down and bottom-up techniques,^{115–118} where these structures find a spectrum of applications including electronics,¹¹⁹ photonics,^{120,121} biotechnology,^{122,123} phononics,¹²⁴ and microfluidics.¹²⁵

Figure 1 shows a schematic diagram of two different thin films coated onto two electrodes with an air gap in between and an electric field applied across them. Unlike the case of a single film where instability generates surface structures, this configuration

(59) Berry, B. C.; Stafford, C. M.; Pandya, M.; Lucas, L. A.; Karim, A.; Fasolka, M. J. *Rev. Sci. Instrum.* **2007**, *78*, 072202.
 (60) Mukherjee, R.; Bandyopadhyay, D.; Sharma, A. *Soft Matter* **2008**, *4*, 2086.
 (61) Higgins, A. M.; Jones, R. A. L. *Nature* **2000**, *404*, 476.
 (62) Léopoldès, J.; Damman, P. *Nat. Mater.* **2006**, *5*, 957.
 (63) Ghatak, A.; Chaudhury, M. K.; Shenoy, V.; Sharma, A. *Phys. Rev. Lett.* **2000**, *85*, 4329.
 (64) Monch, W.; Herminghaus, S. *Europhys. Lett.* **2001**, *53*, 525.
 (65) Shenoy, V.; Sharma, A. *Phys. Rev. Lett.* **2001**, *86*, 119.
 (66) Ru, C. Q. *J. Appl. Phys.* **2001**, *90*, 6098.
 (67) Shenoy, V.; Sharma, A. *J. Mech. Phys. Solids* **2002**, *50*, 1155.
 (68) Ghatak, A.; Chaudhury, M. K. *Langmuir* **2003**, *19*, 2621.
 (69) Sarkar, J.; Shenoy, V.; Sharma, A. *Phys. Rev. Lett.* **2004**, *93*, 018302.
 (70) Gonuguntla, M.; Sharma, A.; Sarkar, J.; Subramanian, S. A.; Ghosh, M.; Shenoy, V. *Phys. Rev. Lett.* **2006**, *97*, 018303.
 (71) Gonuguntla, M.; Sharma, A.; Mukherjee, R.; Subramanian, S. A. *Langmuir* **2006**, *22*, 7066.
 (72) Schäffer, E.; Thurn-Albrecht, T.; Russell, T. P.; Steiner, U. *Nature (London)* **2000**, *403*, 874.
 (73) Schäffer, E.; Thurn-Albrecht, T.; Russell, T. P.; Steiner, U. *Europhys. Lett.* **2001**, *53*, 518.
 (74) Lin, Z.; Kerle, T.; Baker, S. M.; Hoagland, D. A.; Schaffer, E.; Steiner, U.; Russell, T. P. *J. Chem. Phys.* **2001**, *114*, 2377.
 (75) Deshpande, P.; Sun, X.; Chou, S. Y. *Appl. Phys. Lett.* **2001**, *79*, 1688.
 (76) Lin, Z. Q.; Kerle, T.; Russell, T. P.; Schäffer, E.; Steiner, U. *Macromolecules* **2002**, *35*, 3971.
 (77) Lin, Z. Q.; Kerle, T.; Russell, T. P.; Schäffer, E.; Steiner, U. *Macromolecules* **2002**, *35*, 6255.
 (78) Morariu, M. D.; Voicu, N. E.; Schäffer, E.; Lin, Z.; Russell, T. P.; Steiner, U. *Nat. Mater.* **2003**, *2*, 48.
 (79) Xu, T.; Hawker, C. J.; Russell, T. P. *Macromolecules* **2003**, *36*, 6178.
 (80) Xiang, H.; Lin, Y.; Russell, T. P. *Macromolecules* **2004**, *37*, 5358.
 (81) Leach, K. A.; Lin, Z.; Russell, T. P. *Macromolecules* **2005**, *38*, 4868.
 (82) Leach, K. A.; Gupta, S.; Dickey, M. D.; Wilson, C. G.; Russell, T. P. *Chaos* **2005**, *15*, 047506.
 (83) Harkema, S.; Steiner, U. *Adv. Funct. Mater.* **2005**, *15*, 2016.
 (84) Voicu, N. E.; Harkema, S.; Steiner, U. *Adv. Funct. Mater.* **2006**, *16*, 926.
 (85) Wu, N.; Pease, L. F., III; Russel, W. B. *Adv. Funct. Mater.* **2006**, *16*, 1992.
 (86) Arun, N.; Sharma, A.; Shenoy, V.; Narayan, K. S. *Adv. Mater.* **2006**, *18*, 660.
 (87) Dickey, M. D.; Gupta, S.; Leach, K. A.; Collister, E.; Wilson, C. G.; Russell, T. P. *Langmuir* **2006**, *22*, 4315.
 (88) Bae, J.; Glogowski, E.; Gupta, S.; Chen, W.; Emrick, T.; Russell, T. P. *Macromolecules* **2008**, *41*, 2722.
 (89) Voicu, N. E.; Ludwigs, S.; Steiner, U. *Adv. Funct. Mater.* **2008**, *20*, 3022.
 (90) Wu, N.; Russel, W. B. *Nano Today* **2009**, *4*, 180.
 (91) Arun, N.; Sharma, A.; Pattader, P. S. G.; Banerjee, I.; Dixit, H. M.; Narayan, K. S. *Phys. Rev. Lett.* **2009**, *102*, 254502.
 (92) Herminghaus, S. *Phys. Rev. Lett.* **1999**, *83*, 2359.
 (93) Pease, L. F., III; Russel, W. B. *J. Chem. Phys.* **2003**, *118*, 3790.
 (94) Pease, L. F., III; Russel, W. B. *Langmuir* **2004**, *20*, 795.
 (95) Wu, N.; Russel, W. B. *Appl. Phys. Lett.* **2005**, *86*, 241912.
 (96) Wu, N.; Pease, L. F., III; Russel, W. B. *Langmuir* **2005**, *21*, 12290.
 (97) Wu, X. F.; Dzenis, Y. A. *J. Phys. D: Appl. Phys.* **2005**, *38*, 2848.
 (98) Verma, R.; Sharma, A.; Kargupta, K.; Bhaumik, J. *Langmuir* **2005**, *21*, 3710.
 (99) Kim, D.; Lu, W. *Phys. Rev. B* **2006**, *73*, 035206.
 (100) Tomar, G.; Shankar, V.; Sharma, A.; Biswas, G. *J. Non-Newtonian Fluid Mech.* **2007**, *143*, 120.
 (101) John, K.; Thiele, U. *Appl. Phys. Lett.* **2007**, *90*, 264102.
 (102) John, K.; Hänggi, P.; Thiele, U. *Soft Matter* **2008**, *4*, 1183.
 (103) Sarkar, J.; Sharma, A.; Shenoy, V. *Phys. Rev. E* **2008**, *77*, 031604.
 (104) Li, F.; Ozen, O.; Aubry, N.; Papageorgiou, D. T.; Petropoulos, P. G. *J. Fluid Mech.* **2007**, *583*, 347.
 (105) Tseluiko, D.; Blyth, M. G.; Papageorgiou, D. T.; Vanden-Broeck, J.-M. *J. Fluid Mech.* **2008**, *597*, 449.
 (106) Shankar, V.; Sharma, A. *J. Colloid Interface Sci.* **2004**, *274*, 294.
 (107) Craster, R. V.; Matar, O. K. *Phys. Fluids* **2005**, *17*, 032104.
 (108) Bandyopadhyay, D.; Sharma, A.; Thiele, U.; Reddy, P. D. S. *Langmuir* **2009**, *25*, 9108.

(109) Roberts, S. A.; Kumar, S. *J. Fluid Mech.* **2009**, *631*, 255.
 (110) Yoon, J.; Ru, C. Q.; Midouchowski, A. *J. Appl. Phys.* **2005**, *98*, 113503.
 (111) Shenoy, V.; Sharma, A. *Langmuir* **2002**, *18*, 2216.
 (112) Sarkar, J.; Shenoy, V.; Sharma, A. *Phys. Rev. E* **2003**, *67*, 031607.
 (113) Chung, J. Y.; Kim, K. H.; Chaudhury, M. K.; Sarkar, J.; Sharma, A. *Eur. Phys. J. E* **2006**, *20*, 47.
 (114) Shenoy, V.; Sharma, A. *J. Mech. Phys. Solids* **2002**, *50*, 1155.
 (115) Kim, J. H.; Seo, M.; Kim, S. Y. *Adv. Mater.* **2009**, *21*, 4130.
 (116) Srinivasarao, M.; Collings, D.; Philips, A.; Patel, S. *Science* **2001**, *292*, 79.
 (117) Bunz, U. H. F. *Adv. Mater.* **2006**, *18*, 973.
 (118) Park, S.; Lee, H.; Han, T. H.; Kim, S. O. *Adv. Funct. Mater.* **2007**, *17*, 2315.
 (119) Karthaus, O.; Adachi, C.; Kurimura, S.; Oyamada, T. *Appl. Phys. Lett.* **2004**, *84*, 4696.
 (120) Hu, X.; An, Q.; Li, G.; Tao, S.; Liu, J. *Angew. Chem., Int. Ed.* **2006**, *45*, 8145.
 (121) Lee, S.-K.; Yi, G.-R.; Moon, J. H.; Yang, S.-M.; Pine, D. J. *Adv. Mater.* **2006**, *18*, 2111.
 (122) Min, E.-H.; Wong, K. H.; Stenzel, M. H. *Adv. Mater.* **2008**, *20*, 3550.
 (123) Wang, L. Y.; Lee, M. H.; Barton, J.; Hughes, L.; Odom, T. W. *J. Am. Chem. Soc.* **2008**, *130*, 2142.
 (124) Leroy, V.; Bretagne, A.; Fink, M.; et al. *Appl. Phys. Lett.* **2009**, *95*, 171904.
 (125) Menges, V.; Josseland, J.; Girault, H. H. *Anal. Chem.* **2002**, *74*, 4279.

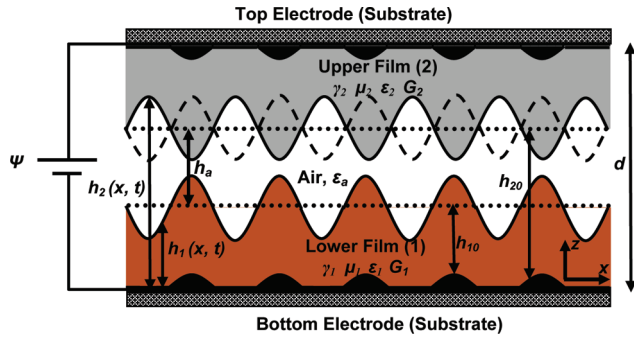


Figure 1. Two-dimensional schematic diagram of two interacting films under the influence of an electric field applied by the two electrodes used as substrates for the films. The mean and local thicknesses of the lower layer are $h_{10} - a_1 f_1(x)$ and $h_1(x, t) - a_1 f_1(x)$, respectively, and the mean and local thicknesses of the upper layer are $[d - a_2 f_2(x)] - h_{20}$ and $[d - a_2 f_2(x)] - h_2(x, t)$, respectively. The symbol h_a is the thickness of the air gap between the two interfaces, and d is the distance between the electrodes. The symbols $\gamma_i, \mu_i, \epsilon_i, G_i$, and ϵ_i are the surface energy, viscosity, shear modulus, and dielectric permittivity of the i th layer. The solid and broken lines at the upper interface indicate squeezing and bending modes of evolution with respect to the solid line at the lower interface, respectively.

allows the possibility of producing 3-D embedded microstructures such as air pockets and channels by allowing the periodic contact of the two unstable free surfaces. In the first part of the study, a linear stability analysis (LSA) is carried out for two interacting viscoelastic films to reveal that changes in the ratios of film thicknesses to material properties (shear moduli, surface tensions, and dielectric permittivities) can significantly alter the length scale and timescale of the instabilities. Following this, a long-wave nonlinear analysis is presented for two interacting viscous layers illustrating the short- and long-time morphologies under different conditions. Simulations reveal that the interfaces always deform in antiphase squeezing mode rather than in in-phase bending mode,^{27,108,126} leading to embedded microstructures. Interesting examples are presented where a change in a kinetic parameter such as viscosity alters only the pathway of evolution but not the final morphology whereas a change in a thermodynamic property such as surface tension could alter both pathways and the equilibrium morphology. Furthermore, the influence of the patterned electrodes on the pathways of evolution and morphology is presented. Two dimensional (2-D) and three dimensional (3-D) nonlinear simulations are used to illustrate the fabrication of a number of interesting periodic patterns such as pincushion structures, embedded microchannels, and entrapped microbubbles (e-molding). Some examples of pattern miniaturization by employing the patterned electrodes are also demonstrated.

II. Problem Formulation

We consider the films to be linear viscoelastic materials¹¹⁴ and carry out LSA on the governing equations of the films to obtain the dispersion relation. The asymptotic cases of purely viscous and purely elastic films can be obtained from the general viscoelastic theory presented here. In addition, the long-wave nonlinear equations for the interfaces are derived for a pair of interacting viscous films, and nonlinear simulations for pattern formation are carried out for this system.

In what follows, x and y are the coordinates parallel to the substrate, z is the coordinate perpendicular to the substrate, and t represents time. Subscript i for the variables denotes the films ($i = 1$ for the lower layer and $i = 2$ for the upper layer), subscript a represents variables associated with the air gap, and superscripts x, y , and z represent the vector components. Symbols $\mathbf{u}_i, \mathbf{v}_i^{(x)}, \mathbf{v}_i^{(y)}, \mathbf{v}_i^{(z)}, \mathbf{n}_i, \mathbf{t}_i, \boldsymbol{\sigma}_i, \kappa_i, P_i (= p_i - \pi_i), \mu_i, G_i$, and γ_i are the displacement, velocity, normal vector, tangent vector, stress tensor, curvature, nonbody force pressure, viscosity, shear modulus and surface energy of the i th layer, respectively. Here p_i and π_i denote the isotropic pressure and excess pressure because of the applied electric field, respectively. The variable heights of the two interfaces are represented by h_1 and h_2 , and the respective base state (mean) heights are h_{10} and h_{20} . Notations $h_a (= h_2 - h_1)$ and $h_3 (= d - h_2)$ correspond to the thicknesses of the air gap and the upper film, respectively. The patterned electrodes are described by the functional form $a_i f_i(x, y)$, where a_i is the amplitude and $f_i(x, y)$ is a periodic function of wavelength λ_i .

1. Two Interacting Viscoelastic Films. *A. Governing Equations.* The constitutive relation $\boldsymbol{\sigma}_i = G_i(\nabla \mathbf{u}_i + \nabla \mathbf{u}_i^T) + \mu_i(\nabla \mathbf{u}_i + \nabla \mathbf{u}_i^T)$, which is a linear combination of a Newtonian damper and a Hookean elastic spring connected in parallel, describes a zero-frequency linearly viscoelastic material. This constitutive relation is particularly applicable to cross-linked polymer films such as cross-linked semisolid poly(dimethylsiloxane) (PDMS) where the material deforms at a decreasing rate under constant stress, asymptotically approaches a steady-state strain, and upon stress removal gradually relaxes to its undeformed state. For this class of material, the equations are written in terms of displacements. In the absence of inertia (justified because of the small thickness), the following equations of motion and the continuity equation describe the dynamics of an incompressible i th elastomeric film:

$$-\nabla P_i + \nabla \boldsymbol{\sigma}_i = 0 \text{ and } \nabla \cdot \mathbf{u}_i = 0 \quad (1)$$

B. Boundary Conditions. At $z = 0$ and $z = d$, no-slip and impermeability boundary conditions ($\mathbf{u}_1 = 0$ and $\mathbf{u}_2 = 0$) are applied. Normal stress balances ($p_1 - \mathbf{n}_1 \cdot \boldsymbol{\sigma}_1 \cdot \mathbf{n}_1 = p_0 - \gamma_1 \kappa_1$ and $-p_2 + \mathbf{n}_2 \cdot \boldsymbol{\sigma}_2 \cdot \mathbf{n}_2 = -p_0 - \gamma_2 \kappa_2$), shear stress balances ($\mathbf{t}_1 \cdot \boldsymbol{\sigma}_1 \cdot \mathbf{n}_1 = 0$ and $\mathbf{t}_2 \cdot \boldsymbol{\sigma}_2 \cdot \mathbf{n}_2 = 0$), and the kinematic conditions ($\dot{h}_1 + (\mathbf{u}_1 \cdot \nabla_s) h_1 = \dot{\mathbf{u}}_1 \cdot \mathbf{n}_1$ and $\dot{h}_2 + (\mathbf{u}_2 \cdot \nabla_s) h_2 = \dot{\mathbf{u}}_2 \cdot \mathbf{n}_2$) are applied at interfaces $z = h_1$ and $z = h_2$.

C. Excess Pressure Induced by an Electric Field. The excess pressures (π_1 and π_2) at the interfaces resulting from the electric field can be obtained by considering the assembly to be a series capacitor.^{72,108,127} The total free energy $\Delta G = -C\psi^2/2$ obtained from the capacitance ($C^{-1} = C_1^{-1} + C_a^{-1} + C_2^{-1}$) is employed to calculate the excess electrical pressures ($\pi_1 = \partial(-\Delta G)/\partial h_1$ and $\pi_2 = \partial(-\Delta G)/\partial(d - h_2)$) at the interfaces:

$$\pi_1 = \left[\frac{\epsilon_0 \epsilon_1 \epsilon_2^2 (\epsilon_1 - 1) \psi^2}{2[\epsilon_2(1 - \epsilon_1)h_1 + \epsilon_1(\epsilon_2 - 1)h_2 + \epsilon_1 d]^2} \right] \text{ and} \quad (2)$$

$$\pi_2 = \left[\frac{\epsilon_0 \epsilon_1^2 \epsilon_2 (\epsilon_2 - 1) \psi^2}{2[\epsilon_2(1 - \epsilon_1)h_1 + \epsilon_1(\epsilon_2 - 1)h_2 + \epsilon_1 d]^2} \right]$$

Here, $C_1 [= \epsilon_0 \epsilon_1 \bar{A}/h_1]$, $C_a [= \epsilon_0 \bar{A}/(h_2 - h_1)]$, and $C_2 [= \epsilon_0 \epsilon_2 \bar{A}/(d - h_2)]$ represent the capacitances of the lower layer, the air gap, and the upper layer, respectively. Symbols \bar{A} , ψ , ϵ_1 , ϵ_2 , and ϵ_0 represent the area of the flat interfaces, the applied voltage, and the dielectric permittivities of the lower layer, the upper layer, and the free space, respectively.

(126) Maldarelli, C. H.; Jain, R. K.; Ivanov, I. B.; Ruckenstein, E. *J. Colloid Interface Sci.* **1980**, *78*, 118.

(127) Griffiths, D. J. *Introduction to Electrodynamics*, 2nd ed.; Prentice Hall: New Delhi, 1989.

D. Linear Stability Analysis. To perform LSA, we assume that the base state is at $\mathbf{u}_i = 0$, $P_i = 0$, $h_i = h_{i0}$ and $\pi_i = \pi_i(h_{i0}, h_{20})$. The LSA is carried out by noting that (i) the kinematics of deformation of the films is treated using a small deformation formulation and (ii) the excess pressures are expanded using Taylor series expansions about their base state and terms up to first order are retained.

$$\begin{aligned} & \pi_1(h_{10} + \delta_1, h_{20} + \delta_2) \\ &= \pi_1(h_{10}, h_{20}) + \left[\left(\frac{\partial \pi_1}{\partial h_1} \right) \bigg|_{h_{10}, h_{20}} \delta_1 + \left(\frac{\partial \pi_1}{\partial h_2} \right) \bigg|_{h_{10}, h_{20}} \delta_2 + \dots \right] \\ & \pi_2(h_{10} + \delta_1, h_{20} + \delta_2) \\ &= \pi_2(h_{10}, h_{20}) + \left[\left(\frac{\partial \pi_2}{\partial h_1} \right) \bigg|_{h_{10}, h_{20}} \delta_1 + \left(\frac{\partial \pi_2}{\partial h_2} \right) \bigg|_{h_{10}, h_{20}} \delta_2 + \dots \right] \end{aligned} \quad (3)$$

where δ_1 and δ_2 are the infinitesimal perturbations at the lower and upper interfaces, respectively. The governing differential equations are linearized using the normal linear modes $\mathbf{u}_i = \tilde{\mathbf{u}}_i e^{\omega t + i k x}$, $P_i = \tilde{P}_i e^{\omega t + i k x}$, and $h_i = h_{i0} + \tilde{h}_i e^{\omega t + i k x}$ where symbols ω and k represent the linear growth coefficient and the wavenumber of disturbance, respectively.

Eliminating $\tilde{u}_i^{(x)}$ and \tilde{P}_i from the linearized governing equations leads to the following biharmonic equations for the i th viscoelastic layer:

$$\frac{d^4 \tilde{u}_i^{(z)}}{dz^4} - 2k^2 \frac{d^2 \tilde{u}_i^{(z)}}{dz^2} + k^4 \tilde{u}_i^{(z)} = 0 \quad (4)$$

The general solution of eq 4 is

$$\tilde{u}_i^{(z)} = (B_{1i} + B_{2i}z)e^{kz} + (B_{3i} + B_{4i}z)e^{-kz} \quad (5)$$

where coefficients B_{ji} ($i = 1$ and 2 and $j = 1-4$) are constants that are to be determined using the boundary conditions. The solution for $\tilde{u}_i^{(z)}$ (eq 5) is used in the governing equations (eq 1) to obtain the expressions for other linearized variables $\tilde{u}_i^{(x)}$ and \tilde{P}_i . Finally, solutions of all of these linearized variables are subsequently used in the boundary conditions to obtain a set of eight homogeneous linear algebraic equations for the eight unknown constants B_{ji} ($i = 1$ and 2 and $j = 1-4$). The determinant of the coefficient matrix is equated to zero to obtain the dispersion relation $\omega = f(k)$ as shown in the Appendix (eq A1). The dominant growth coefficient (ω_m) and the corresponding wavelength ($\lambda_m = 2\pi/k_m$) are obtained by finding the global maxima of ω and the corresponding wavelength ($\lambda = 2\pi/k$) from the general dispersion relation.

2. Two Interacting Viscous Layers. *A. Nonlinear Analysis.* The equations of evolution at the interfaces are obtained under the following set of assumptions: (a) the inertial terms can be neglected because the films are thin and (b) the long-wave approximation is valid because all interfacial deformations have a small slope. As shown by the linear analysis, the long-wave approximation is indeed valid, as is the case for all thin viscous films. Thus, starting with the Navier–Stokes equations in the lubrication approximation $\mu_i v_{iz}^{(x)} = (p_i - \pi_i)_x$ and $\mu_i v_{iz}^{(y)} = (p_i - \pi_i)_y$, the equations of continuity, $\nabla \cdot \mathbf{v}_i = 0$, the kinematic boundary conditions for the individual layers, $h_t + (\mathbf{v}_i \cdot \nabla_s) h_i = \mathbf{v}_i \cdot \mathbf{n}_i$, and the velocity and stress boundary conditions at the two liquid–solid and liquid–air interfaces, we obtain the following coupled equations for the two interfaces in this geometry by following

the standard procedure^{19–21,23–25,30–42,60} employed for the long-wave analysis in thin films:

$$\frac{\partial h_1}{\partial t} = \frac{1}{3\mu_1} \nabla \cdot [(h_1 - a_1 f_1)^3 \nabla P_1] \quad (6)$$

$$\frac{\partial h_2}{\partial t} = \frac{1}{3\mu_2} \nabla \cdot [(h_2 - (d - a_2 f_2))^3 \nabla P_2] \quad (7)$$

The boundary conditions employed are $\mathbf{v}_1 = 0$ at $z = a_1 f_1$ (no slip and impermeability at the lower solid–liquid interface), $\mu_1 v_{1z}^{(x)} = 0$ and $\mu_1 v_{1z}^{(y)} = 0$ at $z = h_1$ (zero shear at the lower liquid–air interface); $\mu_2 v_{2z}^{(x)} = 0$ and $\mu_2 v_{2z}^{(y)} = 0$ at $z = h_2$ (zero shear at the upper liquid–air interface), and $\mathbf{v}_2 = 0$ at $z = d - a_2 f_2$ (no slip and impermeability at the upper solid–liquid interface). The normal stress balances at the two interfaces are used to derive the excess pressures at the respective interfaces

$$P_1 = -\gamma_1 \nabla^2 h_1 - \varepsilon_2 (\varepsilon_1 - 1) \theta + \frac{\beta_1}{(h_1 - a_1 f_1)^5} + \frac{\beta_2}{(h_2 - h_1)^5} \quad (8)$$

$$P_2 = \gamma_2 \nabla^2 h_2 - \varepsilon_1 (\varepsilon_2 - 1) \theta + \frac{\beta_3}{(h_2 - h_1)^5} + \frac{\beta_4}{((d - a_2 f_2) - h_2)^5} \quad (9)$$

where $\theta = (\varepsilon_0 \varepsilon_1 \varepsilon_2 \psi^2)/2[\varepsilon_2(1 - \varepsilon_1)h_1 + \varepsilon_1(\varepsilon_2 - 1)h_2 + \varepsilon_1(d - a_2 f_2) - \varepsilon_2 a_1 f_1]^2$. The last two terms in eqs 8 and 9 are the short-range repulsive potentials introduced to remove the nonphysical singularity at contact lines by introducing a cutoff ultrathin precursor.^{20,32,98,108} We employ a “softer” repulsive potential¹⁰⁸ for ease of numerical computations. The expressions for β_1 and β_2 appearing in eq 8 are obtained by minimizing the free energy [$\pi_1 = \partial(-\Delta G)/\partial h_1 = 0$] at $(h_1 - a_1 f_1) \rightarrow l_0$ and $(h_2 - h_1) \rightarrow l_0$.^{20,32,98,108} Similarly, the expressions for β_3 and β_4 appearing in eq 9 are obtained by minimizing the free energy [$\pi_2 = \partial(-\Delta G)/\partial(d - h_3) = 0$] at $h_2 - h_1 \rightarrow l_0$ and $((d - a_2 f_2) - h_2) \rightarrow l_0$. Here, l_0 is the equilibrium cutoff distance.

The pressures at the interfaces due to the applied electric field, π_1 and π_2 , for unstable interacting films placed on topographically patterned electrodes are functions of the film thickness and spatial coordinates $\pi_i = f(x, y, h_1, h_3)$. The gradient of electrical pressure can thus be written in the following manner as the sum of forces on the film surface arising from two different mechanisms:^{35,36,43}

$$d\pi_i = \frac{\partial \pi_i}{\partial h_1} \bigg|_{x, y, h_3} dh_1 + \frac{\partial \pi_i}{\partial h_3} \bigg|_{x, y, h_1} dh_3 + \frac{\partial \pi_i}{\partial x} \bigg|_{y, h_1, h_3} dx + \frac{\partial \pi_i}{\partial y} \bigg|_{x, h_1, h_3} dy \quad (10)$$

Here, $\alpha|_\beta$ implies a variable α evaluated at constant β . The first two terms in eq 10 represent the forces due to the change in the potential with the variation in the local film thickness, which governs the spinodal instability.^{35,36,43} The last two terms in eq 10 represent the forces due to the change in the potential (at constant upper and lower layer thicknesses) as a result of the physical heterogeneities of the substrate [$\pi_i = f(x, y)$ as shown in Figure 1]. It may be noted that the gradients of potentials, ∇P_1 and ∇P_2 , in eqs 6 and 7 include the force due to the local film thickness variations (the first two terms in eq 10) and also the forces resulting from the imposed spatial heterogeneity of the electric field via its spatial dependence on the surface topography $f(x, y)$ (the last two terms in eq 10). The first component of force, $-(\partial P_i / \partial h_i) \nabla h_i$ at a given location, engenders the well-known spinodal instability for a spatially homogeneous field by causing a flow from the thinner to the thicker regions of the film whenever the spinodal parameter

is negative. This condition is always met for the destabilizing electrostatic field considered here. The second force due to the heterogeneity of the electric field at constant thickness moves the fluid from the low to the high region of the electric field, for example, from the region where the electrode spacing (air gap) is higher to where it is lower. This effect is similar to the movement of a liquid in a thin film from the lower-wettability to higher-wettability regions on a substrate.^{30–42} However, the use of an electric field provides additional and more flexible control strategies for directed movements of a fluid and its patterning compared to wettability control by relatively short-ranged van der Waals and other intermolecular interactions, which can be modulated only by a change in the material properties.

B. Solution of the Nonlinear Equations: Numerical Methods. The evolution equations (eqs 6 and 7) are nondimensionalized for a compact representation of numerical results by introducing the following nondimensional parameters

$$t = T \left[\frac{12\mu_1\gamma_1 h_{10}^3}{(\varepsilon_0\psi^2)^2} \right];$$

$$(x, y, \lambda_m, \lambda_b) = (X, Y, \Lambda, \Lambda_b) \left[\left(\frac{2\gamma_1 h_{10}^3}{\varepsilon_0\psi^2} \right)^{1/2} \right];$$

$$(P_1, P_2) = (\bar{P}_1, \bar{P}_2) \left[\frac{\varepsilon_0\psi^2}{2h_{10}^2} \right]$$

with $(h_i, d, a_i, f_i) = (H_i, D, A_i, F_i)h_{10}$, $\gamma_2 = S\gamma_1$, and $\mu_2 = M\mu_1$.

The dimensionless forms of the equations thus obtained are

$$\frac{\partial H_1}{\partial T} = \nabla[(H_1 - A_1 F_1)^3 \nabla \bar{P}_1] \quad (11)$$

$$\frac{\partial H_2}{\partial T} = \frac{1}{M} \nabla[(H_2 - (D - A_2 F_2))^3 \nabla \bar{P}_2] \quad (12)$$

The expressions for the dimensionless normal stress balances are

$$\bar{P}_1 = -\nabla^2 H_1 - \varepsilon_2(\varepsilon_1 - 1)\Theta + \frac{\bar{\beta}_1}{(H_1 - A_1 F_1)^5} + \frac{\bar{\beta}_2}{(H_2 - H_1)^5} \quad (13)$$

$$\bar{P}_2 = S(\nabla^2 H_2) - \varepsilon_1(\varepsilon_2 - 1)\Theta + \frac{\bar{\beta}_3}{(H_2 - H_1)^5} + \frac{\bar{\beta}_4}{((D - A_2 F_2) - H_2)^5} \quad (14)$$

Here, $\Theta = (\varepsilon_1 \varepsilon_2)/[\varepsilon_2(1 - \varepsilon_1)H_1 + \varepsilon_1(\varepsilon_2 - 1)H_2 + \varepsilon_1(D - A_2 F_2) - \varepsilon_2 A_1 F_1]^2$ and $\bar{\beta}_i$ ($i = 1-4$) are the nondimensional expressions for β_i that appear in eqs 8 and 9. Equations 11–14 are discretized in space using a central difference scheme with half-node interpolations. Gear's algorithm is then employed to solve the resulting set of coupled stiff ordinary differential equations in time with a volume-preserving initial random perturbation and periodic boundary conditions in space. Typically, for 2-D (3-D) simulations ~ 300 (30×30) grid points per Λ is employed and the grid independence of the solutions was verified. Unless otherwise noted, typical values of the parameters chosen for the nonlinear simulations are $\varepsilon_0 = 8.85 \times 10^{-12} \text{ C}^2/\text{N m}^2$, $\varepsilon_1 = \varepsilon_2 = 2.5$, $\mu_1 = \mu_2 = 1 \text{ Pa s}$, $\gamma_1 = \gamma_2 = 0.038 \text{ N/m}$, and $\psi = 25 \text{ V}$.

III. Results and Discussion

A static electric field when applied across a thin dielectric material leads to charge separation, which generates electrical stresses at the interfaces. As a stress relaxation measure, the free interfaces become unstable and deform more toward the medium that has lower

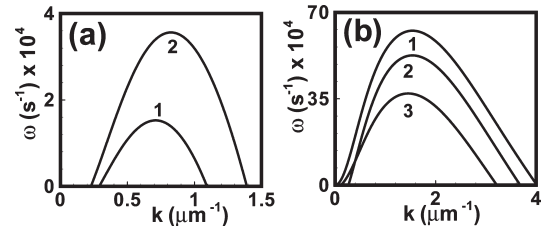


Figure 2. Results obtained from LSA. (a) Curves 1 and 2 show the variation of ω vs k for a set of two interacting viscoelastic films for $\varepsilon_2 = 1$, $h_2 = d = 2.2 \mu\text{m}$, and $d = h_2 = 1.2 \mu\text{m}$. The same curves show the variation of ω with k when a single viscoelastic film is confined between electrodes separated by $d_{\text{sin}} = d = 2.2 \mu\text{m}$ and $d_{\text{sin}} = h_2 = 1.2 \mu\text{m}$, respectively. (b) Curves 1–3 show the variation of ω with k for a set of two interacting viscoelastic films when $G_1 = G_2 = 0$, $G_1 = G_2 = 0.01 \text{ MPa}$, $G_2 = 0.001 \text{ MPa}$, and $G_1 = 0.1 \text{ MPa}$, respectively. For plots a and b, the parameters for two interacting films are $\mu_1 = \mu_2 = 1 \text{ Pa s}$, $\varepsilon_1 = \varepsilon_2 = 3$, $\psi = 200 \text{ V}$, $\gamma_1 = \gamma_2 = 0.03 \text{ N/m}$, $G_1 = G_2 = 0.001 \text{ MPa}$, $d = 2.2 \mu\text{m}$, and $h_1 = d - h_2 = 1 \mu\text{m}$. For the single film, the parameters are $\mu = 1 \text{ Pa s}$, $\varepsilon = 3$, $\psi = 200 \text{ V}$, $\gamma = 0.03 \text{ N/m}$, $G = 0.001 \text{ MPa}$, $h = 1 \mu\text{m}$, and $d_{\text{sin}} = 2.2 \mu\text{m}$.

dielectric permittivity. Thus, the interfaces of a pair of interacting films (shown in Figure 1) always deform toward the air gap under the influence of an external electric field. The length scale and timescale of such instabilities are determined by the relative strengths of the destabilizing (e.g., electric field) and stabilizing forces (e.g., surface tension and elasticity) present in the films. In the first part of this section, we discuss the results obtained from the linear stability analysis of two interacting viscoelastic films. Thereafter, with the help of 2-D and 3-D nonlinear simulations we uncover a number of interesting features of the interfacial deformations of a pair of interacting viscous films.

1. Linear Stability Analysis of Interacting Viscoelastic Films. In this section, we examine the variations of the growth rate (ω) and wavelength (λ) of the instability with ratios of the thickness ($h_r = h_1/h_3$), dielectric permittivity ($\varepsilon_r = \varepsilon_1/\varepsilon_2$), and surface tension ($\gamma_r = \gamma_1/\gamma_2$) of the films.

Figure 2a shows the growth rate (ω) versus wavenumber (k) curves from the general dispersion relation when the upper film is absent by setting $\varepsilon_2 = 1$ (air; curve 1), $h_2 = d = 2.2 \mu\text{m}$ (curve 1), or $d = h_2 = 1.2 \mu\text{m}$ (curve 2). These curves are found to match ω versus k curves for a single film ($d_{\text{sin}} = d = 2.2 \mu\text{m}$, curve 1; $d_{\text{sin}} = h_2 = 1.2 \mu\text{m}$, curve 2) exactly, thus confirming the asymptotic verification of the analysis. Curves 1–3 in Figure 2b show that when the shear modulus is increased only the dominant growth rate (ω_m) decreases rapidly but the dominant length scale (λ_m) remains invariant. Importantly, ω versus k plots (e.g., curves 2 and 3) indicate that the interacting elastomer layers are unstable only for a range of nonzero wavenumbers under the influence of an electric field. The larger wavenumber modes are stabilized by the surface tension force, and the smaller wavenumber modes ($k \rightarrow 0$) are stabilized by the elastic force.¹¹⁴ In contrast, for viscous interacting films (curve 1), very small wavenumber modes ($k \rightarrow 0$) are also unstable because of the lack of elasticity in the system. As observed for single films,¹¹⁴ for the interacting layers the major effect of film elasticity is to shrink the window of unstable wavenumbers and reduce the magnitude of the growth rate. It is important to note here that the instabilities in the interacting layers grow by picking up the dominant wavelength of instability rather than the subdominant very long wavenumber modes, which can be stabilized by the elastic forces present in the films. Therefore, the morphological evolutions for both viscous and viscoelastic films are expected to be the same; however, the reduced growth rate of instability for the interacting layers with viscoelastic solid enforces a larger time requirement for

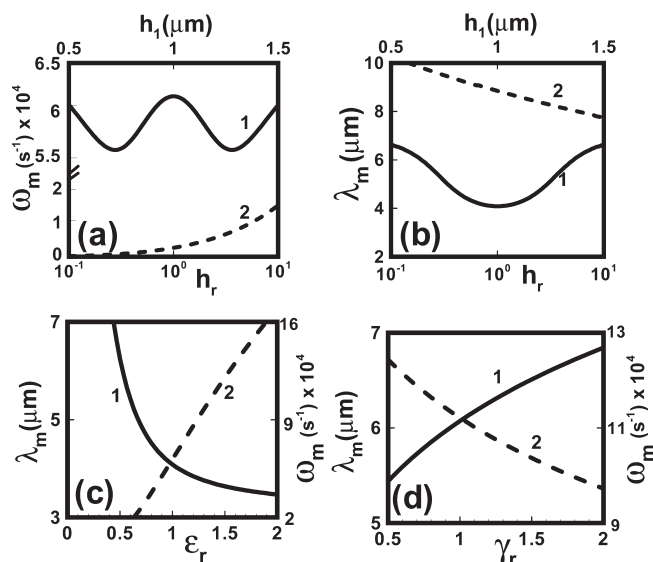


Figure 3. Results obtained from LSA. (a, b) Variations of ω_m and λ_m , respectively, with h_r (at constant h_a and d , curve 1) and h_1 (at constant d and $d - h_2 = 0$, $G_1 = G_2 = 0$, curve 2). Curve 2 essentially represents a single viscous film in plots a and b. (c, d) Variations of λ_m (curve 1) and ω_m (curve 2), respectively, with ϵ_r (at constant ϵ_2) and γ_r (at constant γ_2). (a–d) $\mu_1 = \mu_2 = 1$ Pa s, $\epsilon_1 = \epsilon_2 = 3$, $\psi = 200$ V, $\gamma_1 = \gamma_2 = 0.03$ N/m, $G_1 = G_2 = 0.001$ MPa, $d = 2.2$ μm , $h_1 = d - h_2 = 1$ μm , and $h_a = 0.2$ μm . (d) $\gamma_2 = 0.015$ N/m, $h_1 = 0.05$ μm , $h_2 = 0.25$ μm , and $d = 0.3$ μm .

fabricating similar patterns as compared to that of the viscous interacting layers. The nonlinear simulations presented in the subsequent sections for a pair of interacting viscous films are qualitatively similar to the morphological behavior of an interacting soft viscoelastic film to the extent that the dominant mode of instability is long-wave. Electric-field-induced instabilities with very highly destabilizing electric field (e.g., very high voltage) can show short-wave instabilities, and our nonlinear analysis ceases to be valid in that regime.

The variations of the dominant growth coefficient (ω_m) and the corresponding wavelength (λ_m) of the instability with the ratios of various parameters are summarized in Figure 3. The solid line in Figure 3a shows that when the applied voltage (ψ), the distance between the electrodes (d), and the air gap between the films (h_a) are kept constant and only the ratio of the film thicknesses (h_r) is varied, ω_m is maximized at $h_r = 1$. The Figure also shows that, on either side of $h_r = 1$, ω_m initially decreases, reaches a minimum, and then increases at very high or low h_r . This change in the growth rate can be ascribed to the change in the compliance (defined by the ratio of the thickness to the shear modulus (h/G) of a film) of the films because at constant ψ , d , h_a , γ_i , and G_i the compliance of the films is the only parameter that varies with the change in film thickness. Thus, a reduction (increment) in ω_m takes place because of the decreasing (increasing) compliance of the thinner (thicker) film with the change in h_r . The solid line in Figure 3b shows that λ_m is minimized when $h_r = 1$ and it progressively increases on either side of $h_r = 1$. This is because when $h_r < 1$ or $h_r > 1$ the influence of the surface tension is more pronounced in the thinner film, which increases the values of λ_m . In addition, an increase in the thickness of one of the films also contributes to the increase in λ_m . This is in accordance with the previous single-film studies where it was shown that for both elastic and viscoelastic films the wavelength of instability increases with film thickness because of the smaller energy penalty for surface deformation.^{70,71} Interestingly, the broken line in Figure 3b also shows that if one of the films is absent (a single-film system) then λ_m

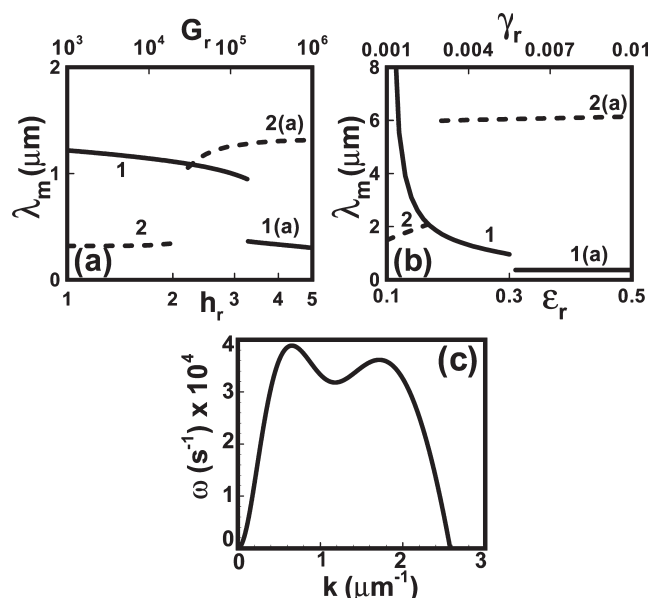


Figure 4. Results obtained from LSA. (a, b) Variation of λ_m with h_r [(a), curves 1 and 1(a)], G_r [(a), curves 2 and 2(a)], ϵ_r [(b), curves 1 and 1(a)], and γ_r [(b), curves 2 and 2(a)]. (c) Typical bimodal ω vs k curve when $h_r = 3.2$. (a–c) $\mu_1 = 1$ Pa s, $\mu_2 = 0.1$ Pa s, $\epsilon_1 = 3$, $\epsilon_2 = 10$, $\psi = 250$ V, $\gamma_1 = 0.04$ N/m, $\gamma_2 = 0.003$ N/m, $G_1 = 0$, $G_2 = 0.025$ MPa, $d = 0.6$ μm , $h_1 = 0.16$ μm , and $d - h_2 = 0.05$ μm .

increases significantly, indicating that the instability produces much smaller structures in the interacting two-film system as compared to those in a similar single-film system. This reduction in wavelength can be attributed to the increased capacitance and hence a stronger destabilizing electric field due to the presence of the second film. Thus, the two interacting film configurations also open up the possibility of fabricating more compact surface patterns on viscous and viscoelastic films as compared to those on the single-film system. Figure 3c,d shows that λ_m decreases (curves 1) and ω_m grows (curves 2) progressively upon increasing the dielectric permittivity or decreasing the interfacial tension of any of the films, owing to an increase (decrease) in the strength of the destabilizing (stabilizing) forces.

Figure 4 shows a special case where the ω versus k plots show the presence of two maxima (bimodality) corresponding to two different locally dominant wavenumbers. The curves in Figure 4a,b show that with changes in the h_r , ϵ_r , G_r , and γ_r ratios, curves for ω_m and λ_m show discontinuities. We observe that at this discontinuity the subdominant (dominant) maximum becomes dominant (subdominant) and a switching of wavelength from shorter (longer) to longer (shorter) takes place. Around this zone of discontinuity, the two modes of a bimodal ω versus k plot are equally strong (Figure 4c) and can lead to instabilities where the interfaces may evolve in two different wavelengths and lead to different equilibrium morphologies at the interfaces. Similar phenomena have already been observed for thin viscous bilayers under air.¹⁰⁸ Thus, to fabricate ordered patterns on the films, the parameter set h_r , ϵ_r , G_r , and γ_r is to be chosen in such a manner that they are far from the zone of bimodality where both interfaces select a single dominant mode and thus evolve in a synchronous manner.

2. Evolution of Instability in Interacting Viscous Films. In this section, we discuss the 2-D and 3-D nonlinear evolution of the interfaces. In particular, we show the pathways of evolution and the resulting morphologies for the interacting viscous layers. It is important to note that the final morphologies shown here are not always the steady-state or near-equilibrium morphology. In most cases, to preserve the interesting microstructures we exclude the late-stage coalescence and the loss of ordering because of that. The

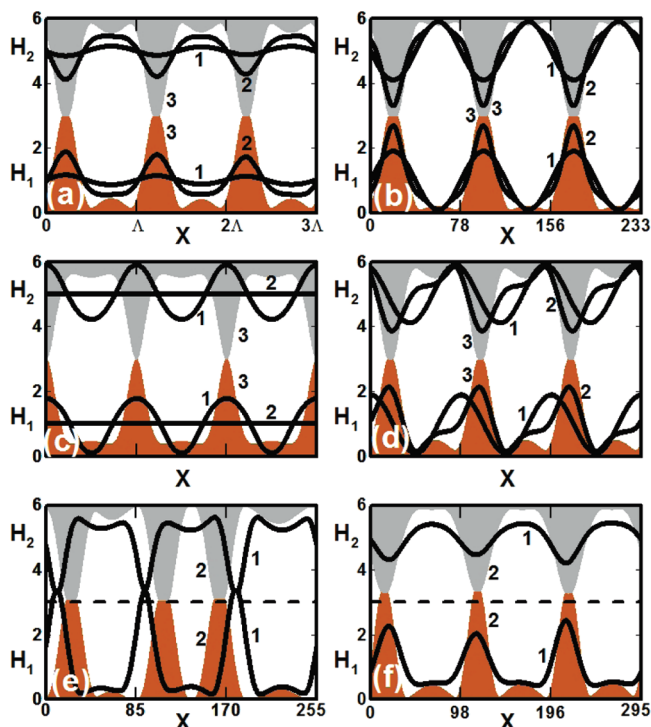


Figure 5. Two-dimensional nonlinear evolution of interfaces in the $L = 3\Lambda$ domain. The initial perturbations imposed in the images are (a) random, (b) antiphase squeezing mode, (c) in-phase bending mode, (d) slightly out-of-phase bending mode, and (e, f) random. Curves 1–3 corresponds to (a) $T = 1.5 \times 10^5$, 1.8×10^5 , and 2.7×10^5 ; (b) $T = 0$, 2.4×10^3 , and 6.8×10^4 ; (c) $T = 0$, 3.7×10^5 , and 6.1×10^5 ; and (d) $T = 0$, 2.1×10^4 , and 7.8×10^4 . (e) Evolution when $\mu_1 = 0.2$ Pa s and $\mu_2 = 1.0$ Pa s. Curves 1 and 2 represent $T = 4.2 \times 10^5$ and 2.0×10^6 . (f) Evolution when $\gamma_1 = 0.02$ N/m and $\gamma_2 = 0.06$ N/m. Curves 1 and 2 represent $T = 3.2 \times 10^5$ and 6.0×10^5 . The broken lines in images e and f are drawn midway between the two electrodes. For all cases, $h_{10} = 1 \mu\text{m}$, $d - h_{20} = 1 \mu\text{m}$, and $d = 6 \mu\text{m}$.

ordering observed for the simulations can experimentally be realized by freezing the structures in the intermediate stage of evolution.

A. Morphologies on Homogeneous Planar Electrodes. Figure 5 shows the 2-D nonlinear simulations of a pair of interacting viscous films resting on homogeneous electrodes. Image a shows that the interfaces reorganize into an antiphase squeezing mode (curves 1 and 2) within a short time. Interestingly, the upward columns formed in the lower and downward columns formed in the upper layer originate at the same spatial location and meet each other midway through the air gap (curve 3). The formation of columns in the films occurs in synchronization because the growth of the column in one layer increases the electrical stress locally at the same x - y spatial location on the other layer. Thus, the growth of a column in the lower (upper) layer promotes the growth of a column in the upper (lower) layer in a coupled manner. It is also interesting that the final morphology shown in Figure 5, curve 3 of image a, does not depend on the initial conditions. For example, curves 1–3 in image b show that when the initial perturbation is in squeezing mode the same morphology still develops, but in a shorter time span. In contrast, when the initial perturbation is in the in-phase bending mode (image c, curve 1), the surface tension forces dominate the electrical stresses and the liquid–air interfaces first become nearly flat (image c, curve 2) before reverting to the squeezing mode and the final morphology (image c, curve 2) is again similar to images a and b. Image d shows a scenario when the initial perturbation is in the marginally out-of-phase bending mode, which again leads to the same morphology as

obtained in the previous cases. Image e indicates that apart from the initial conditions, even when the kinetic parameters such as viscosity are largely different in the two films, the final morphology remains the same (curve 2)! It is important to note that when the viscosities of the films are different, the columns formed at short time are not the same size (curve 1) in the upper and lower layers because the growth rate of the columns is controlled by the viscous forces in the initial stages of evolution. However, near equilibrium, the heights of the downward and upward columns appear to be the same (curve 2). The simulations clearly show that although the pathway of evolution can be controlled by kinetic factors the final morphology is always controlled by thermodynamic parameters only. This is further proved by the simulation shown in image f. In this case, the interfaces have different surface energies and the final morphology shows that the columns appear to be taller (shorter) in films with less (more) surface energy.

The 2-D simulations shown in Figure 5 do not show the complete picture of the evolution because the effects of out-of-plane curvature and flow are not considered. In Figure 6, we show the 3-D nonlinear evolution of a pair of interacting viscous films in a $4\Lambda \times 4\Lambda$ domain. Interfaces initially deform in squeezing mode (images in row A) at short times. As the evolution progresses, the columns in the lower and upper layers grow toward each other because of the enhanced electric-field-engendered stresses at these locations (images in rows B and C). The final morphology consists of an array of upward columns in the lower layer and downward columns in the upper layer, meeting each other exactly at the middle of the air gap (images in row D). The final morphology in Figure 6 shows a randomly distributed 3-D structure as compared to the periodic structures observed in the 2-D simulations shown in Figure 5. The structures shown in row D can be of some technological importance because they would produce surfaces with random physical heterogeneity if one of the layers is selectively removed. The electric-field-induced pincushion-like structures thus generated on each film surfaces can potentially be employed to fabricate functional surfaces for superwetting and so forth. It is also interesting to note here that when both the films are composed of the same material we expect the columns to merge and form pillarlike structures in between the two interacting films. This particular morphology can have potential applications as a (i) porous shock-absorbing layer and (ii) a microfluidic structure for applications in dielectrophoresis and rapid mixing.

B. Morphologies on Topographically Patterned Electrodes. Figure 6 shows that the structures in films placed on flat electrodes are rather limited in the type of structures that can be formed. In this section, we demonstrate that long-range order in the final morphologies can be generated when the electrodes are topographically patterned. In general, when a ridgelike pattern is fabricated on any of the electrodes or both electrodes, the effective distance between electrodes decreases in the zones where these ridges are present. The increase in the local strength of the electric field forces, as a result of the local lowering of the gap between the electrodes, directs the evolution pathway. The 2-D nonlinear simulations in images a and b in Figure 7 show that when either of the electrodes or both electrodes are patterned, the final morphologies (curve 2) faithfully follow the patterns decorated on the electrodes. In particular, image b shows that when one of the electrodes is fabricated with patterns of periodicity of $\Lambda/2$ the final morphology still faithfully follows the length scale of the pattern on the electrode rather than the spinodal length scale. Thus, employing patterned electrodes with pattern periodicities of less than the spinodal length scale can lead to pattern miniaturization. Image c shows another strategy for the fabrication of miniaturized patterns by employing phase-shifted electrodes, each of which has a pattern

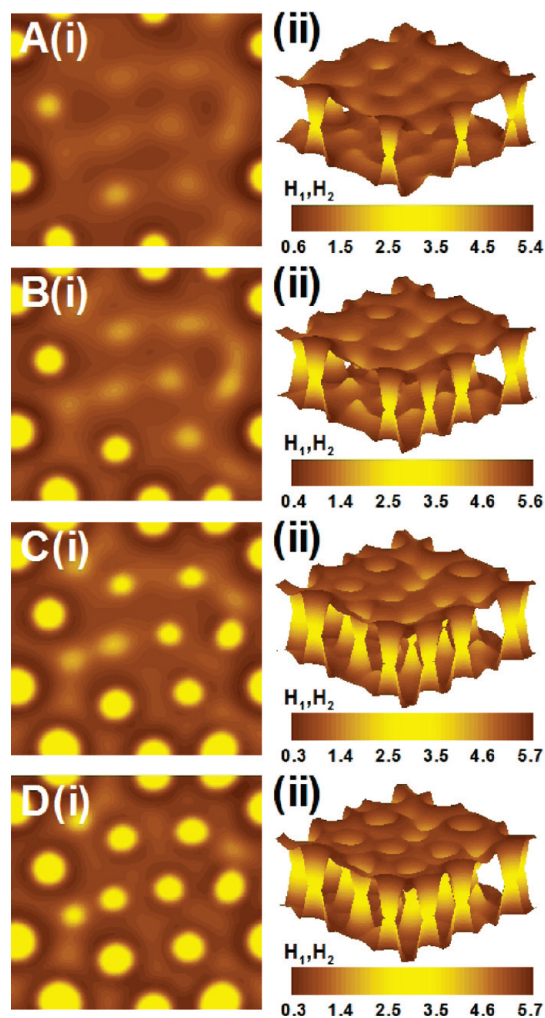


Figure 6. Three-dimensional nonlinear evolution of interfaces in the $L = 4\Lambda \times 4\Lambda$ domain. The films are placed over flat electrodes. Images i in both image rows show the contour diagram of the film surfaces, and images ii show the 3-D surface profiles. The profiles are shown at (A) $T = 15.4 \times 10^4$, (B) $T = 16.4 \times 10^4$, (C) $T = 17.3 \times 10^4$, and (D) $T = 17.8 \times 10^4$. In this case, $h_{10} = 1 \mu\text{m}$, $d - h_{20} = 1 \mu\text{m}$, and $d = 6 \mu\text{m}$. Lighter shades in the images represent thicker regions in the films.

periodicity of Λ . In this case, the patterns on the electrodes are kept out of phase. The interfacial morphologies follow the patterns fabricated on the electrodes, and columnar structures with a periodicity of $\Lambda/2$ can be fabricated on the film surfaces. It is important to note here that the miniaturization of patterns is possible when either of the electrodes is patterned or both of the electrodes are patterned with a periodicity that is less than the spinodal length scale. However, there are exceptions to this finding. For example, when the air gap between the films is relatively thick, the film surfaces do not follow the patterns fabricated on the electrodes. Image d shows that although the films pick a wavelength similar to that of electrode patterning at short times, the final morphology reverts to the spinodal length scale.

Figures 8–10 show the 3-D nonlinear structures that evolve on patterned electrodes. Figure 8 shows the spatiotemporal evolution of an interacting system when the films are separated by a thick air gap. When either of the electrodes, as shown in images i–iii in row A, or both electrodes (not shown here) are decorated with an array of periodic striped patterns, the columnar structure appears at the places where the stripes are present. However, the periodicity of the columns

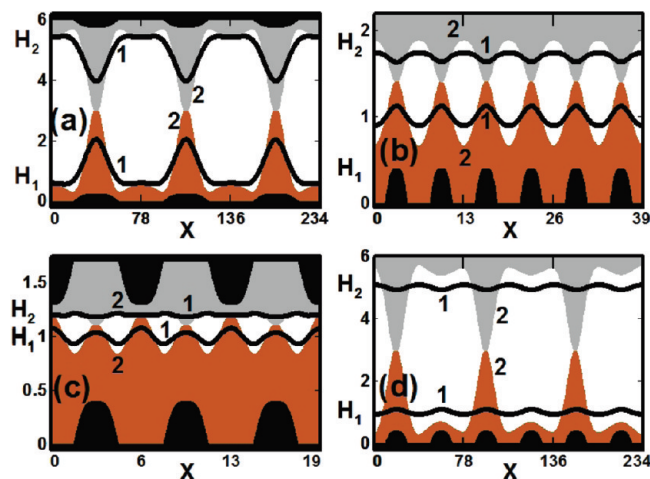


Figure 7. Two-dimensional nonlinear evolution of interfaces in the $L = 3\Lambda$ domain. (a, c) Both substrates are patterned with $\Lambda_b = \Lambda$. (b, d) Only the lower substrate is patterned with $\Lambda_b = 0.5\Lambda$. (a) $a_1 = a_2 = 0.25h_{10}$, $h_{10} = 1 \mu\text{m}$, $d - h_{20} = 1 \mu\text{m}$, and $d = 6 \mu\text{m}$. (b) Substrates are placed in a staggered arrangement, $a_1 = 0.4h_{10}$, $h_{10} = 1 \mu\text{m}$, $d - h_{20} = 0.5 \mu\text{m}$, $d = 2.2 \mu\text{m}$. (c) $a_1 = a_2 = 0.4h_{10}$, $h_{10} = 1 \mu\text{m}$, $d - h_{20} = 0.5 \mu\text{m}$, and $d = 1.7 \mu\text{m}$. (d) $a_1 = 0.4h_{10}$, $h_{10} = 1 \mu\text{m}$, $d - h_{20} = 1 \mu\text{m}$, $d = 6 \mu\text{m}$. Curves 1 and 2 represent (a) $T = 4.4 \times 10^4$ and 5.9×10^4 ; (b) $T = 6.0$ and 24.5 ; (c) $T = 0.15$ and 0.58 ; and (d) $T = 1.6 \times 10^4$ and 2×10^5 .

follows the spinodal length scale along the stripes in the longitudinal direction. Images i–iii in row B show that upon patterning both electrodes with periodic striped patterns placed orthogonally to each other (cross-striped), columns appear at the intersection of the two stripes, which are also the points of smallest distance between the two electrodes. Upon cross patterning one of the electrodes (not shown here) or both electrodes (images i–iii in row C), columnar structures appear exactly above the locations where the ridges are fabricated on the electrodes. Thus, perfect periodic ordering of structures on the films is observed in contrast to the random patterns generated on homogeneous substrates (Figure 6, image row D).

Figure 9 shows the spatiotemporal evolution for similar configurations as shown in Figure 8, but with a thinner air gap. When striped patterns are placed on either of the electrodes (images i–iii in rows A and B) or both the electrodes (not shown here), the columnar structure appears but coalesces within a short time to form continuous walls, leaving behind cavities along the length, and is out of phase with the pattern stripes. On cross-striped or cross-patterned electrodes (images i–iii in rows B and C), the coalescence of columns results in continuous structures with entrapped cavities at the interstitial spaces between the substrate patterns. The simulations in Figure 9 indicate that this type of configuration can be employed for micromolding of a periodic array of embedded microchannels (row A) or embedded microbubbles (rows C and D). Thus, the proposed e-field lithography with two films can be used to fabricate a variety of imbedded patterns, in contrast to the use of a single film that produces only surface patterns.

A number of other interesting morphologies can also be e-molded. Figure 10 shows some examples of cases in which the electrodes are patterned with intricate patterns. Images i–iii in row A show that patterning the electrodes with ridges of periodicity $\Lambda/2$ leads to the pattern on the film surface, also with a periodicity of $\Lambda/2$, that points to the miniaturization of patterns on the film surface compared to the spinodal length scale. This 3-D image corresponds to the 2-D simulation shown in Figure 7b. Images i–iii in row B demonstrate that meandering microchannels¹²⁵ can also be fabricated on the film surfaces when the electrodes are decorated with a zigzag striped pattern. The meanderings in the microchannels

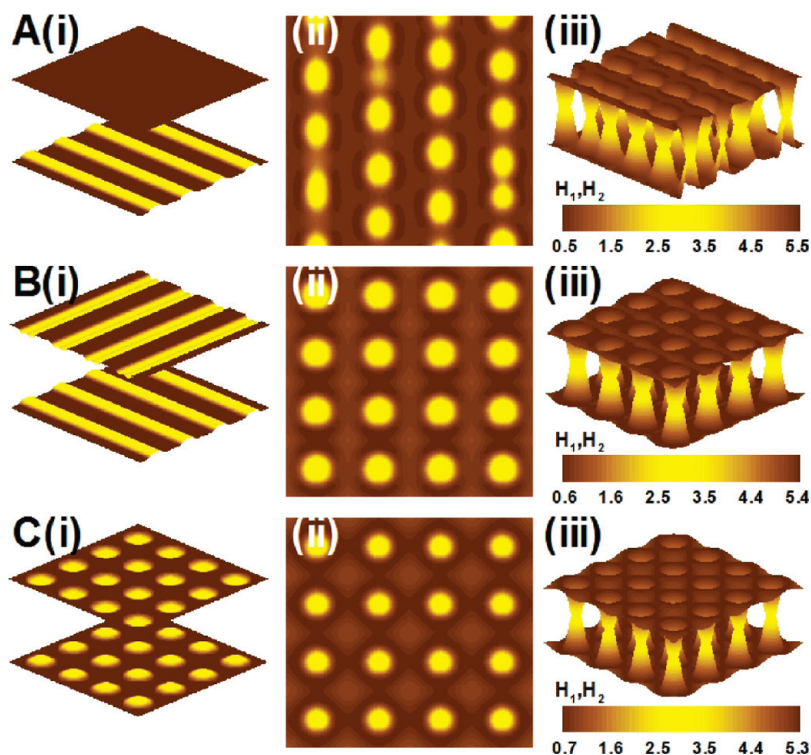


Figure 8. Three-dimensional nonlinear evolution of the interfaces in the $L = 4\Lambda \times 4\Lambda$ domain. The films are placed over patterned substrates. Images i in all of the image rows show the patterning on the substrates, images ii show the contour diagram of the film surfaces, and images iii show the 3-D surface profiles. The profiles are shown at (A) $T = 6.5 \times 10^4$, (B) $T = 5.8 \times 10^4$, and (C) $T = 3.5 \times 10^4$. For all cases, $h_{10} = 1 \mu\text{m}$, $d - h_{20} = 1 \mu\text{m}$, $d = 6 \mu\text{m}$, $\Lambda_b = \Lambda$, and $a_1 = a_2 = 0.25h_{10}$. Lighter shades in the images represent thicker regions in the films.

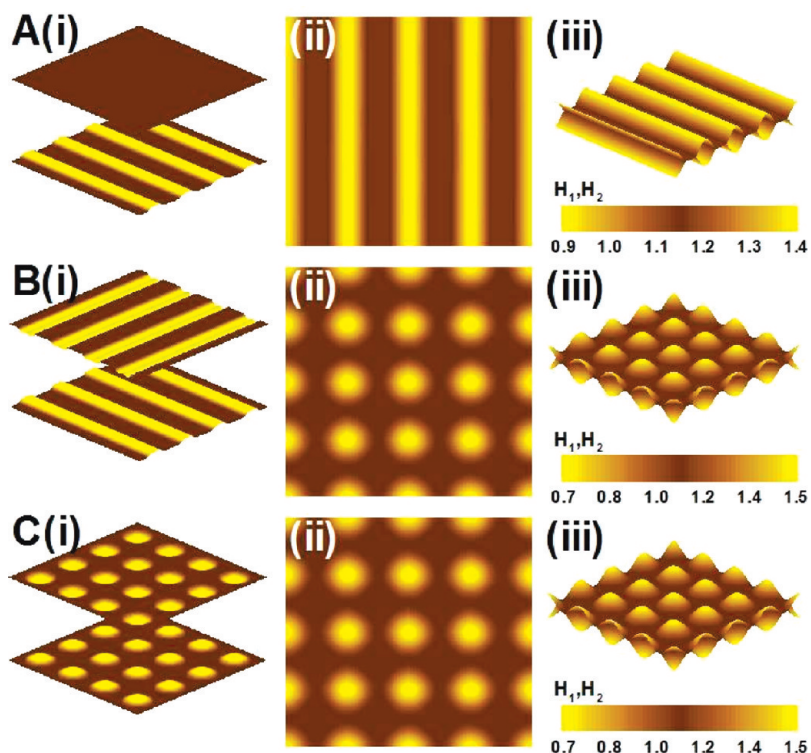


Figure 9. Three-dimensional nonlinear evolution of the interfaces in the $L = 4\Lambda \times 4\Lambda$ domain. The films are placed over patterned substrates. Images i in all of the image rows show the patterning on the substrates, images ii show the contour diagram of the film surfaces, and images iii show the 3-D surface profiles. The profiles are shown at (A) $T = 2.4$, (B) $T = 8.8$, and (C) $T = 7.3$. For all cases, $h_{10} = 1 \mu\text{m}$, $d - h_{20} = 1 \mu\text{m}$, $d = 2.2 \mu\text{m}$, $\Lambda_b = \Lambda$, and $a_1 = a_2 = 0.25h_{10}$. Lighter shades in the images represent thicker regions in the films.

could be useful in microfluidics aimed at rapid micromixing. Images i–iii in row C show a possible microreactor configuration with a central cavity connected to inlet and outlet channels. Figure 10

points to the fact that the interacting films' configuration has the potential to fabricate a number of intricate self-organized meso-patterns that are otherwise difficult to fabricate.

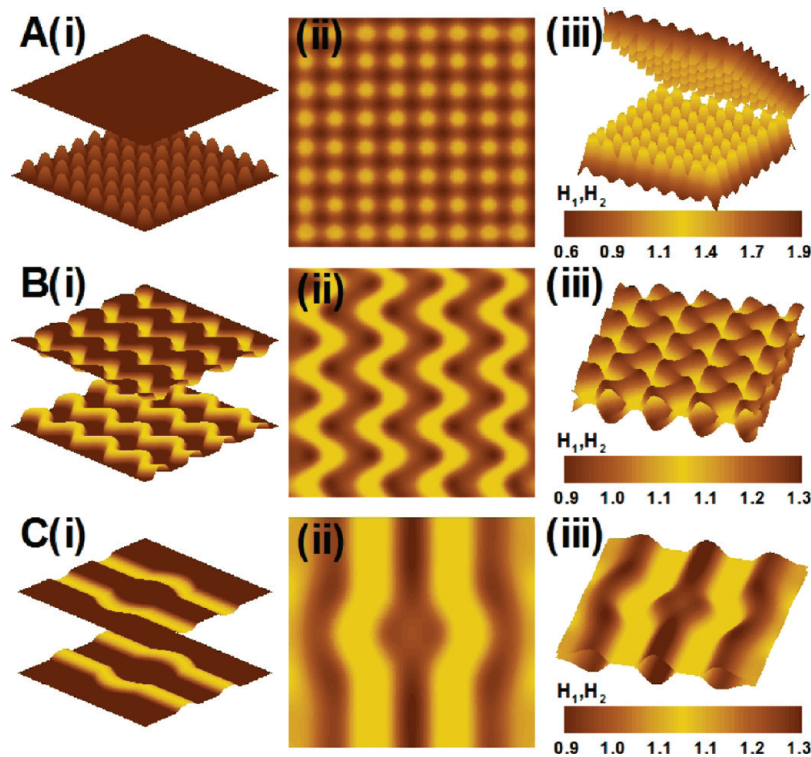


Figure 10. Three-dimensional nonlinear evolution of the interfaces. The films are placed over patterned substrates. Images i in all of the image rows show the patterning on the substrates, images ii show the contour diagram of the film surfaces, and images iii show the 3-D surface profiles. (A) $h_{10} = 1 \mu\text{m}$, $d - h_{20} = 0.5 \mu\text{m}$, $d = 2.2 \mu\text{m}$, $\Lambda_b = 0.5\Lambda$, $a_1 = 0.4h_{10}$, and the profile is shown at $T = 70.2$. (B, C) $h_{10} = 1 \mu\text{m}$, $d - h_{20} = 1 \mu\text{m}$, $d = 2.2 \mu\text{m}$, $\Lambda_b = \Lambda$, $a_1 = a_2 = 0.25h_{10}$, and the profiles are shown at $T = 0.62$ and 2.85 , respectively. (A, B) The domain length is $L = 4\Lambda \times 4\Lambda$. (C) The domain length is $L = 3\Lambda \times 3\Lambda$. Lighter shades in the images represent thicker regions in the films.

IV. Conclusions

We show that electric-field-induced instabilities in two interacting films separated by a thin air gap can be directly used to fabricate embedded ordered patterns in polymer films such as arrays of bubbles and channels. The nonlinear simulations reveal that the interfaces always deform in antiphase squeezing mode rather than in in-phase bending mode, leading to embedded microstructures. The initial small defects/perturbations do not influence the final equilibrium morphology, making the method robust. The periodicity of patterns produced by two interacting films is significantly smaller than the periodicity of patterns in a similar single-film system. Additionally, the length scale and timescale of instability can be tuned by changing the ratios of shear moduli, film thickness, interfacial tension, and dielectric properties of the films. Thus, a number of intricate patterns with a wide range of periodicity can be obtained. Furthermore, the simulations demonstrate that although the evolution pathways and kinetics can be altered by changing kinetic parameters such as the viscosity, the final morphology is always dictated by the equilibrium thermodynamic conditions. Thus, once the parameters involving thermodynamic properties are fixed, the final morphology remains invariant. The periodicity and order of the embedded structures can be controlled by varying the air gap, film thickness, and nature and periodicity of the pattern on the electrodes. For example, by varying the spacing between the columns for pincushion-like structures, film surfaces with diverse degrees of structural wetting can be obtained. Several interesting self-organized periodic morphologies such as pincushion-like structures, straight and twisted embedded microchannels, embedded microbubbles and microcavities connected to the inlet and outlet can thus be e-molded by employing appropriately patterned electrodes. Structures with periodicities that are much less than the spinodal length can also be fabricated on patterned electrodes. Examples are

shown for the conditions when the self-organized structures do or do not follow the underlying patterns on the electrodes.

Acknowledgment. We acknowledge the financial support of the Department of Science & Technology, India (IRHPA grant) and the Ministry of Education, Science and Technology, South Korea under the World Class University (WCU) Program (R32-2008-000-20082-0).

Appendix

The dispersion relation for two interacting layers:

$$\begin{vmatrix}
 i & \frac{i}{k} & -i & \frac{i}{k} & 0 & 0 & 0 & 0 \\
 1 & 0 & 1 & 0 & 0 & 0 & 0 & 0 \\
 2ikJ_1J_4 & 2iJ_1J_4J_{12} & \frac{2ikJ_4}{J_1} & \frac{2iJ_4J_{13}}{J_1} & 0 & 0 & 0 & 0 \\
 -J_1J_{10} & -h_1J_1J_{10} & \frac{J_{11}}{J_1} & \frac{h_1J_{11}}{J_1} & -J_2\phi_2 & -h_2J_2\phi_2 & -\frac{\phi_2}{J_2} & -\frac{h_2\phi_2}{J_2} \\
 0 & 0 & 0 & 0 & 2ikJ_2J_5 & 2iJ_2J_5J_{22} & \frac{2ikJ_5}{J_2} & \frac{2iJ_5J_{23}}{J_2} \\
 -J_1\phi_3 & -h_1J_1\phi_3 & -\frac{\phi_3}{J_1} & -\frac{h_1\phi_3}{J_1} & -J_2J_{20} & -h_2J_2J_{20} & \frac{J_{21}}{J_2} & \frac{h_2J_{21}}{J_2} \\
 0 & 0 & 0 & 0 & iJ_3 & \frac{iJ_{31}J_3}{k} & -\frac{i}{J_3} & -\frac{iJ_{32}}{kJ_3} \\
 0 & 0 & 0 & 0 & J_3 & dJ_3 & \frac{1}{J_3} & \frac{d}{J_3}
 \end{vmatrix} = 0 \quad (\text{A1})$$

where $J_1 = e^{kh_1}$, $J_2 = e^{kh_2}$, $J_3 = e^{kd}$, $J_4 = (G_1 + \omega\mu_1)$, $J_5 = (G_2 + \omega\mu_2)$, $J_{10} = (2kJ_4 + \phi_1)$, $J_{11} = (2kJ_4 + \phi_1)$, $J_{12} = (1 + kh_1)$, $J_{13} = (-1 + kh_1)$, $J_{20} = (2kJ_5 + \phi_4)$, $J_{21} = (2kJ_5 + \phi_4)$, $J_{22} = (1 + kh_2)$, $J_{23} = (-1 + kh_2)$, $J_{31} = (1 + kd)$, $J_{32} = (-1 + kd)$, $\phi_1 = \partial\pi_1/\partial h_1$, $\phi_2 = \partial\pi_1/\partial h_2$, $\phi_3 = \partial\pi_2/\partial h_1$, and $\phi_4 = \partial\pi_2/\partial h_2$.